

Novel Analytical Modelling Tools for the Optimization of Micro-resistojet Thruster Performance

Parameswaran, A.; Cervone, A.

DOI

10.52202/078379-0001

Publication date

Document VersionFinal published version

Published in

52nd IAF Student Conference - Held at the 75th International Astronautical Congress, IAC 2024

Citation (APA)

Parameswaran, A., & Cervone, A. (2024). Novel Analytical Modelling Tools for the Optimization of Microresistojet Thruster Performance. In *52nd IAF Student Conference - Held at the 75th International Astronautical Congress, IAC 2024* (pp. 1-15). (Proceedings of the International Astronautical Congress, IAC). International Astronautical Federation, IAF. https://doi.org/10.52202/078379-0001

Important note

To cite this publication, please use the final published version (if applicable). Please check the document version above.

Copyright

Other than for strictly personal use, it is not permitted to download, forward or distribute the text or part of it, without the consent of the author(s) and/or copyright holder(s), unless the work is under an open content license such as Creative Commons.

Takedown policy

Please contact us and provide details if you believe this document breaches copyrights.

We will remove access to the work immediately and investigate your claim.

Green Open Access added to TU Delft Institutional Repository 'You share, we take care!' - Taverne project

https://www.openaccess.nl/en/you-share-we-take-care

Otherwise as indicated in the copyright section: the publisher is the copyright holder of this work and the author uses the Dutch legislation to make this work public.

IAC-24,E2,1,1,x84841

Novel Analytical Modelling Tools for the Optimization of Micro-resistojet Thruster Performance

A. Parameswaran **

^a Faculty of Aerospace Engineering, Delft University of Technology, Kluyverweg 1, 2629 HS Delft, Netherlands, advaitparam@gmail.com

Abstract

With a growing trend in the miniaturisation of satellites, there is an increasing need to develop micro-propulsion systems for these satellites. Since scaling down conventional propulsion systems is challenging and not always possible, new concepts need to be developed. These concepts, although often based on already known systems and principles, require significant modifications to make them meet the requirements of miniaturized propulsion. One such concept is the micro-resistojet, using an electrical resistance to increase the propellant temperature. At Delft University of Technology, two thrusters based on this concept were developed: the Vaporized Liquid Micro-resistojet (VLM) and the Low-Pressure Micro-resistojet (LPM), which were specifically designed for being demonstrated on-board a PocketQube satellite. To determine the operating regime of the thrusters for this demonstration, there is a need to develop simplified analytical models that accurately predict their performance without significant computational expenses. Although there were previous attempts to model these thrusters, they did not provide a complete representation of their performance. For the VLM thruster, the focus of the model presented in this paper was on coupling the heating chamber and the nozzle, to obtain a more accurate value for the mass flow rate through the thruster. The heating chamber section was discretized into finite one-dimensional cells and convective heat transfer equations were used to model parameters such as density, pressure, wall temperature and heat transfer coefficient. The nozzle was modelled based on ideal rocket theory corrected with adequate loss factors. The mass flow rate was calculated iteratively by coupling the two sections until it reached convergence. For the LPM thruster, the focus was on including an accommodation coefficient to account for heat transfer efficiency between thruster walls and propellant. Rarefied gas dynamics equations were used to calculate performance parameters due to the low-pressure conditions within the thruster. The models proved to produce realistic results when compared to available numerical and experimental values, although still with some limitations in modelling heat transfer, which could not be fully overcome yet due to the lack of available data for validation. Optimal operating points were determined for both thrusters by maximizing an objective function based on performance parameters such as thrust-to-power ratio, specific impulse, and mass flow rate. Constraints included thrust, power, and temperature requirements, which led to different optimal points for the thrusters under varying operational conditions.

Keywords: propulsion, micro-resistojet, heat transfer, fluid flow

Nomencla	ature		I_{sp}	Specific impulse	[s]
A_{ht}	Area of heat transfer	$[m^2]$	Kn	Knudsen number	
а	Arbitrary constant		k	Boltzmann constant	
b	Arbitrary constant		k_{cond}	Thermal conductivity	[W/mK]
C_d	Discharge coefficient		L	length	[m]
C_p	Specific heat capacity	[J/kg.K]	L_{lin}	Linear length	[m]
С	Arbitrary constant		l_{nd}	Slant length	[m]
$D_{channel}$	Channel diameter	[m]	L_{tot}	Total (Actual) length	[m]
D_h	Hydraulic diameter	[m]	m_a	Molecular mass	[kg]
d_1	Channel outer diameter	[m]	ṁ	Mass flow rate	[kg/s]
d_2	Channel inner diameter	[m]	$\delta \dot{m}$	Infinitesimal mass flow rate value	[kg/s]
F	Thrust	[N]	Nu	Nusselt number	
${g}_0$	Gravitational acceleration	$[m/s^2]$	n	Arbitrary constant	
Н	Height	[m]	n_{bends}	No. of bends	
h (or h_b)	Heat transfer coefficient	$[W/ms^2K]$	$n_{channel}$	No. of channels	

IAC-24,E2,1,1,x84841 Page 1 of 15

^{*} Corresponding Author

P	Pressure	[Pa]
P_{cs}	Perimeter of cross-section	[m]
Pr	Prandtl number	[]
Ò	Heat transfer rate	[W]
R	Characteristic gas constant	[J/K/mol]
Re	Reynolds number	[3/11/11101]
r_c	Radius of curvature	[m
S	Position value	[m]
T	Temperature	[K]
T_{int}	Internal temperature	[K]
T_{tr}	Translational kinetic temperature	[K]
TP_{ratio}	Thrust-to-power ratio	. ,
δt	Time duration	[s]
и	X-component of velocity	[m/s]
W	Width	[m]
W_c	Centre-to centre distance	[m]
$W_{channel}$	Width of channel	[m]
W_{l_i}	Weights for objective of LPM thruster model with index \$i\$	
W_{nc}	Width of nozzle entry	[m]
W_{nd}	Width of nozzle exit	
vv_{nd}	Weights for objective of VLM	[m]
W_{v_i}	thruster model with index i	
x	Dryness fraction	
α	Transmission coefficient	
α_{acc}	Accommodation coefficient	
Δ	Change in physical quantity	
λ	Molecular mean-free path	[m]
ρ	Density	$[kg/m^3]$
γ	Specific heat ratio	
δ *	Compressible displacement thickness	[m]
η_u	Isp-efficiency	
ф	Aspect ratio	
θ	Compressible momentum thickness	[m]
Σ	Summation	
σ_t	Surface tension	[N/m]
μ	Dynamic viscosity	[Pa-s]
ψ_i	Incident flux	
ψ_r	Reflected flux	
ζ	Degrees of freedom	
Carlagania		

Subscripts:

cs Cross-section

Acronyms/Abbreviations

Wall

Exit

ith Iteration

Liquid phase

Saturated liquid Minimum value

Maximum value

Two-phase flow

Saturated vapor

Vapour phase

Saturated condition Nozzle throat

Silicon

i

l

ls

min max

Si

S

t

tp

v vs

> w 0

DTMP	Dual Thruster Micro-propulsion
FMMR	Free Molecular Micro-resistojet
LEO	Low Earth Orbit
LPM	Low Pressure Micro-resistojet
MEMS	Micro-Electro-Mechanical Systems
obj	Objective function
VLM	Vaporized Liquid Micro-resistojet

Initial value or value at inlet

Nozzle throat parameter (superscript)

Free-stream condition

1. Introduction

Micro-propulsion systems have found a wide application in small-scale satellites, particularly in the case of cubesats. Cubesats are composed of individual units or modules, each with a volume of $10 \times 10 \times 10 \times 10 \times 10$, referred to as 1U. These satellites were initially developed to offer cost-effective access to space [1]. Notably, cubesats offer advantages that include reduced development time and the possibility of launching multiple satellites in a single mission, as opposed to larger satellites. In addition, they provide both spatial and temporal resolution benefits for Earth observation when deployed in large constellations [2]. In 2017, it was demonstrated that cubesats could extend their utility beyond educational purposes to include scientific and exploration missions [3].

To further enhance cost-efficiency and the speed of development, the concept of PocketQubes was introduced at California State Polytechnic University in 2009 [4] with each unit of having a volume of 5 x 5 x 5 cm³, thus, also reducing the space required for launch. However, this compact size implied a need for better energy management. Further, conventional propulsion

IAC-24,E2,1,1,x84841 Page 2 of 15

systems could not be simply scaled down as the governing principles for propulsion systems at smaller scales were significantly different [5]. The challenge was integrating the propulsion system into a confined space, which needed a small-scale propulsion solution.

To address this, two micro-propulsion devices were developed as part of a technology demonstration initiative: the Vaporizing Liquid Micro-resistojet (VLM) thruster and the Low Pressure Micro-resistojet (LPM) thruster [6]. These thrusters had certain advantages when compared to conventional Cold Gas thrusters, as they heated the propellant before expelling it, increasing its energy, resulting in increased thrust. To meet the size, weight, and power constraints imposed by nano-satellites, Micro-Electro-Mechanical Systems (MEMS) were explored as a means of improving the compliance of the system [7].

1.1 Vaporized Liquid Micro-resistojet (VLM) Thruster

A VLM thruster uses the concept of vaporizing a liquid propellant entering the thruster by giving a certain input power and accelerating the propellant through a nozzle to produce the desired thrust. Compared to cold gas thrusters which require to store propellant at high pressures, the heating of the propellant by the resistors meant that the propellant could be stored at a significantly lower pressure. Further, it has the added ability to re-start multiple times [8]. The general setup of a VLM thruster consists of an inlet, a heating chamber and a nozzle. The heating chamber consists of microchannels which can vary in geometry and heater chips adjacent to the chamber that vaporise the propellant, following which it expands out of the nozzle. At TU Delft, a VLM thruster was designed, fabricated and tested by M.D Silva [9] with a different set of geometries. The heating chamber was designed to consist of either microchannels with a serpentine shape or diamondshaped pillars, as shown in Figure 1. Three nozzle configurations were also used of different lengths, as shown in Figure 1.

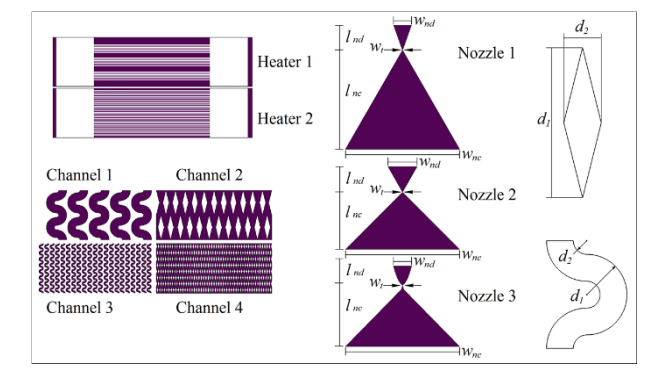


Figure 1. Microchannel geometry used in the work of M.D Silva [9]

1.2 Low Pressure Micro-resistojet (LPM) Thruster

One of the drawbacks of the VLM thruster was the losses that occurred in the micronozzle. To avoid these losses, another option was to run the thruster at low pressure and allow the heat transfer to take place purely due to the collision of the propellant molecules with the wall [5]. This would further help reduce the mass of the system and lower risks of leakage. A concept based on this motivation was developed by Andrew D. Ketsdever [10] in 1998 and was further modified to form the Low Pressure Micro-resistojet (LPM) thruster concept which was developed at TU Delft. The basic configuration consisted of a plenum which operated at a low pressure below 500 Pa wherein the propellant gas would be rarefied. The gas molecules would enter heated slots or channels heated to a constant temperature. The heat transfer to the molecules would occur through collisions with the wall that would increase the energy of the molecules and consequently result in the production of thrust as the molecules exit the thruster.

1.3 Delfi-PQ Technology Demonstration Mission

The Delfi project at TU Delft initially included a nanosatellite project with the objective of providing education, technology demonstration and innovation through the project. The Delfi-C3 mission was the first nanosatellite launched under the Delfi project which was later followed by the Delfi-N3xt nanosatellite [11]. The next step was to develop a PocketQube satellite that could demonstrate payloads which could be made to occupy a much smaller volume. This led to the development of the Delfi-PQ satellite mission at TU Delft with the goal of developing a reliable baseline for innovative payloads and applications that could be demonstrated in orbit.

One of the technology demonstration missions on the Delf-PQ satellite included a Dual Thruster Micropropulsion (DTMP) payload that consisted of the two micro-resistojet thrusters that were to be tested in orbit [6]. The tests were meant to be performed at certain operating points, defined in terms of certain initial conditions, that needed to be pre-determined. With onground experiments, the number of operating points that could be tested was insufficient and likely to be suboptimal. This emphasised the need for theoretical models to accurately predict the thruster performance over a wide range of operating points. Previous models developed for micro-resistojet thrusters represented the performance of the thrusters up to a certain degree of accuracy. However, they did not provide a complete representation of the workings of the thrusters.

There was hence, a need to develop a complete analytical model for both the VLM and LPM thrusters to provide an estimate of their performance over a wide

IAC-24,E2,1,1,x84841 Page 3 of 15

range of input parameters. The current paper focusses on understanding the shortcomings of previously developed models for micro-resistojet thrusters in order to improve the accuracy of the model predictions.

2. Theory and model setup

The fundamental equations used to describe the performance of the two thrusters are based on the rocket thrust equation. However, due to the difference in flow regimes for the two thrusters, the equations used for modelling their performance are considered separately in Sections 1.12.1 and 2.2 for the VLM and LPM thrusters, respectively.

2.1 Modelling the VLM thruster

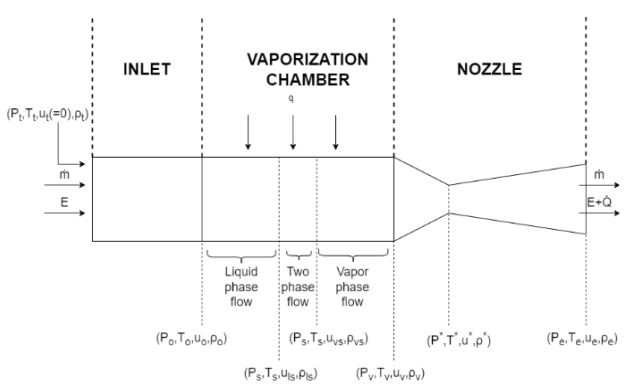


Figure 2. Schematic diagram of the VLM thruster model

A schematic of the VLM thruster model is provided in Figure 2 which includes three distinct sections. The pressure, temperature, velocity and density are represented at various sections of the thruster by the terms P, T, u and p, respectively with appropriate subscripts. The phase of flow gradually changes from liquid to vapour with a region of two-phase flow in between. The input heat flow rate, Q_i , is applied through the thruster walls with an initial temperature, T_{w0} . The propellant is initially stored at a pressure, P_t and temperature T_t in the tank and its flow is regulated by a valve into the inlet to maintain a target mass flow rate. As the propellant enters the chamber, it heats up causing an increase in its temperature. There is also a corresponding increase in the wall temperature adjacent to the fluid. This heating process takes place until the fluid reaches its saturation temperature, at which point vaporization begins. The fraction of vapour (or dryness fraction) at this point is zero and gradually increases to one when all liquid is converted to vapour. It is to be noted that although the temperature and pressure do not vary in this region, there is a significant change in the density and velocity of propellant from ρ_{ls} to ρ_{vs} and from u_{ls} to u_{vs} , respectively. Once fully vaporised, the fluid's temperature continues to increase and attains a temperature T_{ν} at a pressure P_{ν} . The vaporised propellant

then enters the nozzle and is accelerated to reach sonic flow at the throat and expand out with an exit velocity u_e .

2.1.1 Convective Heat Transfer

The VLM thruster's performance is based on the principle of convection which allows the calculation of the amount of heat transferred to the propellant through the walls of the thruster. This can be done with the help of Equation (1) [12].

$$\dot{Q} = (T_s - T_{\infty}) \int_A h \ dA \tag{1}$$

The heat transfer coefficient h is a proportionality constant in the equation that depends on the geometry and properties of the surface material, type of flow and fluid [13]. These parameters are taken into consideration using non-dimensional quantities, especially using the Nusselt number represented by Equation (2).

$$Nu = \frac{h}{c_p} k_{cond} \tag{2}$$

The Nusselt number represents the ratio of the convective heat transfer to the conductive heat transfer and so a higher value would imply a larger heat transfer through convection [12]. For different flow conditions, the Nusselt number has been estimated to be a function of the Reynolds number Re and the Prandtl number Pr in the form shown in Equation (3). The arbitrary constants a, b and c in the Equation may vary based on the flow conditions and were determined through several experiments in previous research.

$$Nu = a(Re)^b (Pr)^c \tag{3}$$

2.1.2 Quasi-1D heating chamber model

The heat transfer occurring in the chamber from the wall to the fluid is modelled as a steady-state 1D model similar to the work of C.A.J Hanselaar [14]. It was noted that due to the presence of a two-phase flow, it was important to predict when the phase change took place. Hence, an iterative procedure was used which included positional increments traversing the length of the chamber. At each increment, the increase in fluid temperature and the corresponding increase in wall temperature due to the incoming heat flux were calculated based on Equations (4) and (5), respectively. Once the saturation temperature had been reached, the dryness fraction at each incremental position was calculated as per Equation (6), until all the liquid was vaporized. Once superheated vapour was formed, the temperature increase was calculated again until the exit of the chamber was reached, i.e., the entire length of the chamber had been traversed. The conditions at the exit were then used as the conditions at the inlet of the nozzle.

IAC-24,E2,1,1,x84841 Page 4 of 15

$$T_{i+1} = T_i + \frac{h_{b_i} \cdot A_{ht} \cdot \left(T_{w_i} - T_i\right) \cdot \frac{\Delta S}{L_{tot}}}{\dot{m} \cdot C_{p_i}} \tag{4}$$

$$T_{w_{i+1}} = T_{w_i} + \frac{(P_{in} - \dot{Q}_t) \cdot \Delta t}{C p_{Si} \cdot m}$$

$$\tag{5}$$

$$x_{i+1} = x_i + \frac{h_{b_i} \cdot A_{ht} \cdot \left(T_{w_i} - T_i\right) \cdot \frac{\Delta s}{L_{tot}}}{m.L} \tag{6}$$

The heat transfer coefficient for single-phase flow was modelled in terms of the Nusselt number. The most suitable correlation for *Nu* was Equation (7) derived by Peng and Peterson [15] for rectangular microchannels in the laminar regime.

$$Nu = 0.1165 \left(\frac{D_h}{W_c}\right)^{0.81} \phi^{0.79} Re^{0.62} Pr^{0.33}$$
 (7)

For two-phase flow, the instability caused by backflow into the inlet of the thruster added to the liquid droplets that may be present at the chamber exit was considered too unpredictable to be considered in a theoretical model and was not looked into in detail. Hence, a weighted average method was chosen to calculate the parameters for the two-phase flow section by taking values calculated for the liquid and vapor phase flows. An example for the density, ρ , is shown in Equation (8).

$$\rho_{i+1} = x_{i+1}.\rho_v + (1 - x_{i+1}).\rho_l \tag{8}$$

2.1.3 Nozzle loss factors

To account for certain losses occurring in the nozzle of a thruster, certain loss factors are considered to better represent the actual performance. The discharge coefficient and Isp-efficiency were considered in the model for the nozzle section. The discharge coefficient was represented as a function of the width of the nozzle throat, the radius of curvature at the throat, and the specific heat ratio of the propellant, as shown in Equation (9). This was based on the work of Kuluva and Hosack [16] that was further applied to develop a 1-D model for micronozzles by D. Fontanarosa [17].

$$C_d = \left(\frac{r_c + 0.05(0.5W^*)}{r_c + 0.75(0.5W^*)}\right)^{0.019} \cdot \left(1 - \frac{r_c + 0.10(0.5W^*)}{0.5W^*}\right)^{0.21} \cdot \left(\frac{1}{P_{01}}\right)^{0.5} \cdot (0.97 + 0.86\gamma)$$
(9)

The Isp-efficiency was defined as a function of the displacement and momentum thickness based on the derived expression for a planar nozzle by Whitfield [18], as given in Equation (10).

$$\eta_u = 1 - \frac{2\delta^*}{W_e} \cdot \left(1 + \frac{\theta}{\delta^*}\right) \tag{10}$$

The correlations for the discharge coefficient and the Ispefficiency were chosen based on their validity for the chosen geometry and operating conditions, as well as their verifiability with previous results.

2.1.4 Coupled model

The main aim of the model was to couple the heating chamber and nozzle sections by using an iterative method to calculate the mass flow rate. To couple the two sections of the thruster, an arbitrary value for the mass flow rate is initially assumed at the inlet of the thruster and its value is iteratively calculated until convergence is reached. The mass flow rate at the nozzle throat is also calculated and is compared with the initial assumed value. If the difference in values is less than an arbitrary limit δm , then the value is assumed to have converged. Else, the mass flow rate value is updated and the process is repeated iteratively. Using the converged value of mass flow rate in the rocket thrust equation allows the thrust and specific impulse produced to be calculated. A flowchart representing this method is shown in Figure 3. Flowchart explaining the methodology of the coupled

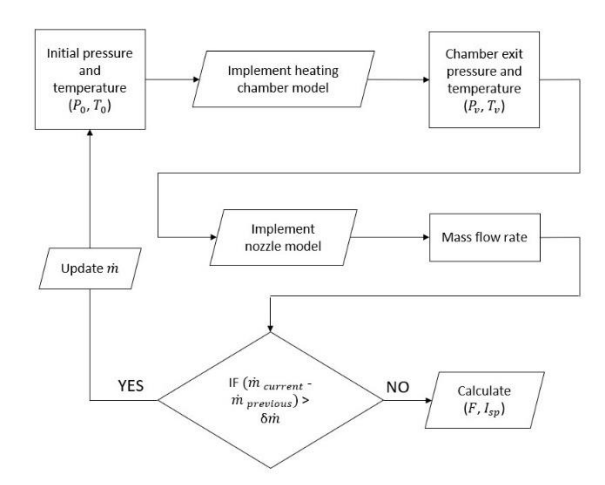


Figure 3. Flowchart explaining the methodology of the coupled model

2.2 Modelling the LPM thruster

The basic configuration consisted of a plenum which operated at a low pressure below 500 Pa wherein the propellant gas would be rarefied. The gas molecules would then enter heated slots or channels heated to a constant temperature. The heat transfer to the molecules would occur through collisions with the wall that would increase the energy of the molecules and consequently result in the production of thrust as the molecules exit the thruster. An illustration of the work is shown in Figure 4. The velocity of the particles entering the slot is represented with c while the velocity of molecules at the exit is shown as c'. Few molecules may re-enter the plenum after collision with a velocity c'' [19].

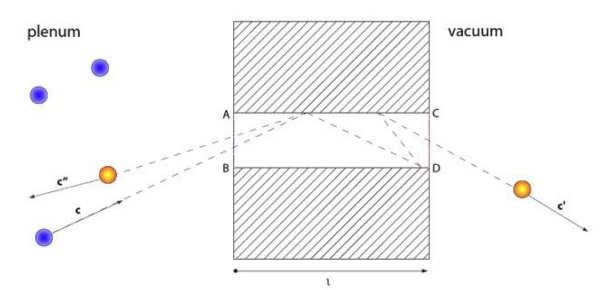


Figure 4. Schematic diagram of the working principle of the LPM thruster. [20]

The LPM thruster was modelled based on Maxwell's distribution function provided in Equation (11) [21].

$$f(u,v,w) = \left(\frac{m_a}{2\pi kT}\right)^{3/2} e^{-\frac{m_a(u^2 + v^2 + w^2)}{2kT}}$$
(11)

The translational kinetic temperature of the gas molecules is a measure of its translational kinetic energy and was defined as a function of the wall temperature, as shown in Equation (12) [20]. This was further used to calculate the exit velocity as shown in Equation (13) and consequently, the thrust as in Equation (14).

$$T_{tr} = \frac{6\gamma}{\pi + 6\gamma} T_w \tag{12}$$

$$u_e = \sqrt{\frac{\pi \cdot k \cdot T_{tr}}{2m_a}} \tag{13}$$

$$F = \alpha . P_0 . A_e \frac{\pi + 2}{2\pi} \sqrt{\frac{T_w}{T_0} \frac{6\gamma}{\pi + 6\gamma}}$$
 (14)

To account for the loss in the thrust due to the reflection of a certain number of molecules back into the plenum of the thruster, the transmission coefficient was considered. It represents the ratio of the number of molecules exiting from the outlet of the thruster to that entering the heater chip. It depends on the geometry used in the thruster and was found to be a function of the aspect ratio, ϕ , of the slot or channel [22]. The definition of the coefficient for the slot and channel geometries are given in Equations (15) and (16), respectively.

$$\alpha = 0.5(1 + \sqrt{1 + \phi^2} - \phi) - \frac{1.5(\phi - \ln(\phi + \sqrt{1 + \phi^2})^2)}{\phi^3 + 3\phi^2 + 4 - (\phi^2 + 4)\sqrt{1 + \phi^2}}$$
(15)

$$\alpha = 1 + (\phi^2) - \phi \sqrt{\phi^2 + 1} - \frac{\left((2 - \phi^2) \sqrt{\phi^2 + 1} + \phi^3 - 2 \right)^2}{4.5\phi \sqrt{\phi^2 + 1} - 4.5 ln(\phi + \sqrt{\phi^2 + 1})} \tag{16}$$

To account for the heating effect of the thruster in the calculation of the performance parameters, an accommodation coefficient, defined in Equation (17) was considered which gives a measure of the efficiency with

which momentum and energy are transferred from the walls of the thruster to the gas molecules.

$$\alpha_{acc} = \frac{\psi_r - \psi_i}{\psi_w - \psi_i} \tag{17}$$

This is represented as a ratio of the difference in incident and reflected flux of the molecules to the ideal difference in flux between the wall and the incident molecules [23]. As per the work of Liang Tengfei [24], the coefficient could also be expressed as given in Equation (18).

$$\alpha_{acc} = \frac{u_0^2 - u_e^2}{u_0^2 - \frac{4kT_W}{m_a}} \tag{18}$$

Further simplification shows that the accommodation coefficient is purely a function of the thermal properties of the propellant, as per Equation (19).

$$\alpha_{acc} = \frac{6\gamma}{\pi + 6\gamma} \tag{19}$$

3. Results and Discussion

3.1 Results for the VLM thruster model

The preliminary geometry assumed was based on the work of M.D Silva [9] Among the configurations worked on, the serpentine channel, from Figure 1, was arbitrarily chosen to test the working of the model. Figure 5 shows a single bend of the channel consisting of curved sections with the inner and outer diameters labelled along with the channel diameter. The values of these geometrical parameters are listed in Table 1.

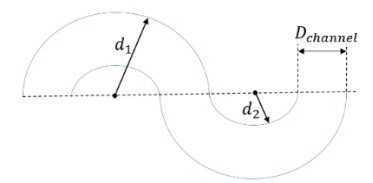


Figure 5. Section of serpentine channels in the chamber

Table 1. Geometrical parameters of heating chamber

	Small serpentine	Large serpentine
$\Delta s (\mu m)$	1	1
L_{lin} (μm)	900	900
$W_{channel}\left(\mu m\right)$	44.4	44.4
d_1 (μm)	76.6	266
$d_2(\mu m)$	0.00001	0.0001
n_{bends}	55	14
$n_{channel}$	21	5

^{*} $\mu m = \text{Microns}$

IAC-24,E2,1,1,x84841 Page 6 of 15

Table 2. Geometrical parameters of the nozzle

	Short nozzle	Long nozzle
$A^* (m^2)$	2e-09	2e-09
Area ratio	17	11
W_{nc} (μm)	3000	3000
W_{nd} (μm)	780	500
$l_{nd}~(\mu m)$	660	645

The propellant used was water vapour based on the trade-off study performed by D.C Guerrieri et. al. [25] wherein a selected set of potential propellants were compared based on their performance, safety, density, flammability and instability. The material of the wall of the heating chamber section was considered to be Silicon as it was the material used during the fabrication of the thruster at TU Delft. [9]

The pressure and temperature at the inlet were assumed to be 5 bar and $300~\rm{K}$, respectively. The saturation temperature of water at this pressure was calculated to be $424.98~\rm{K}$.

3.1.1 Temperature profile

The temperature profile through the length of the chamber was also plotted for all four configurations, as shown in Figure 6. The corresponding wall temperature profile was also plotted. Near the inlet of the chamber, it was observed that the chamber temperature steeply increased in an almost linear manner until the onset of the two-phase flow. However, there was an initial drop in wall temperature following which there was an increase in a linear manner similar to the chamber temperature. This was likely due to the large difference in temperature between the wall and the fluid at the inlet. It was further observed that complete vaporisation occurred faster for the short nozzle configurations, as seen in Figure 6c and Figure 6d. This could be attributed to the higher mass flow rates for the short nozzle configurations that would give less time for the fluid to be vaporised within the chamber.

This also resulted in the chamber temperature converging relatively more towards the wall temperature near the exit of the chamber for the long nozzle configurations compared to the short nozzle. This would imply that thermal equilibrium was reached faster in the case of the long nozzle. In reality, complete vaporisation may occur at a later position than predicted due to factors not considered and it may be useful to have the onset of vapor flow as early as possible.

The convergence of the mass flow rate for the coupled model was also monitored in each case and took

around 4 to 5 iterations on average to converge. Based on the results obtained for certain geometry and operating conditions, the analytical model showed realistic results with expected values of thrust and specific impulse for a micro-propulsion system.

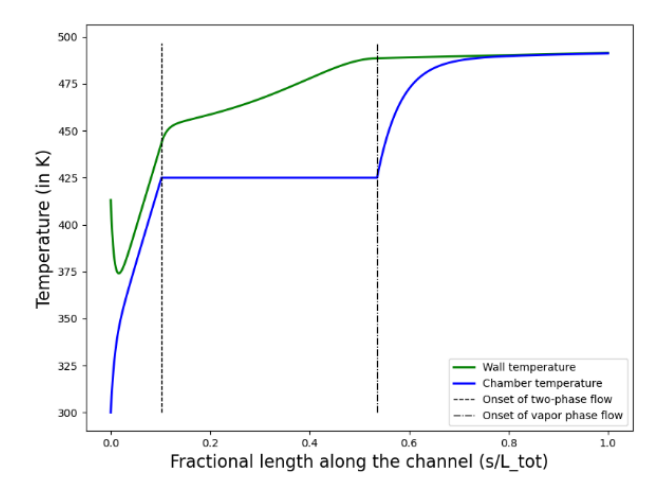


Figure 6a. Large serpentine - Long nozzle

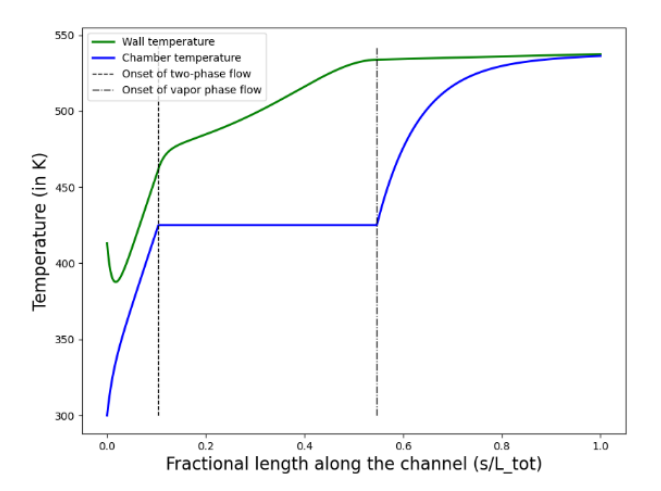


Figure 6b. Small serpentine — Long nozzle

Wall temperature — Chamber temperature — Chamber temperature — Onset of two-phase flow — Onset of vapor phase flow — Onset of vapor phase flow — Onset of vapor phase flow — Fractional length along the channel (s/L tot)

Figure 6c. Large serpentine - Short nozzle

IAC-24,E2,1,1,x84841 Page 7 of 15

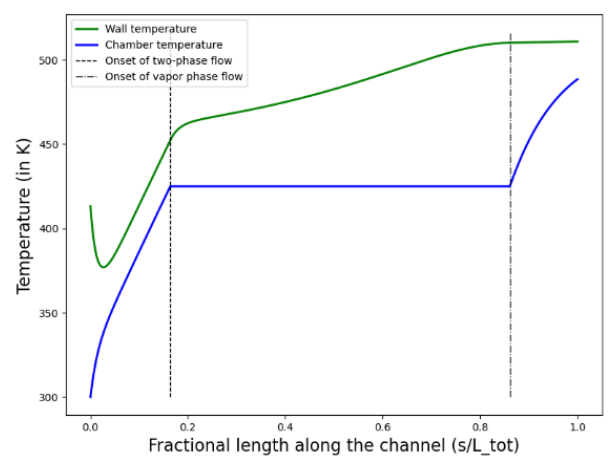


Figure 6d. Small serpentine - Short nozzle

Figure 6. Temperature profile of propellant and walls in the heating chamber

3.1.2 Effect of operating conditions on thruster performance

To understand the sensitivity of the model to operating conditions, it was useful to understand the variation of the thruster performance over a larger domain of operating temperatures, pressures and input power values. To start with, the effect of the chamber exit pressure and temperature on the thrust, specific impulse and mass flow rate produced was analysed as this focused on the predictions of the nozzle model alone. It was observed that high pressure was required to provide more thrust while a higher chamber temperature favoured the specific impulse.

The effect of the inlet pressure and temperature at the entrance of the heating chamber on the performance of the thruster was also analysed by varying the pressure between 1 to 6 bar and the temperature between 300 and 500 K. The input power was varied between 1 and 9 W. The resulting contours of the temperature at the chamber exit for input powers of 1 W, 4 W and 9 W, respectively, were plotted as shown in Figure 7.

A clear observation from the plots is the sudden change in contour levels beyond a particular inlet temperature. This was likely due to the fact that the propellant at the inlet was assumed to be fully vaporised when its temperature was above the saturation point for a given inlet pressure. This meant that the heat that would have been used to vaporise the fluid was now used to further increase the chamber temperature. However, the region above the saturation point would not have practical use as the propellant would enter the chamber as a liquid. At inlet temperatures below the saturation conditions, the chamber exit temperature decreases as the inlet pressure is increased. This could be explained by the fact that the saturation temperature increases with an

increase in chamber pressure. This would cause more heat to be used to increase the temperature of the liquid, which has a higher heat capacity than the vapour phase.

Another observation was that there was a much steeper decrease in exit temperature below the inlet saturation point in Figure 7c. This was because the higher power allowed for a greater increase in vapour temperature after the fluid had reached its saturation point. Moreover, a higher input power caused the wall temperature to also increase, which in turn increased the fluid temperature even more.

A similar pattern is observed when plotting the contours of the performance parameters as a function of the inlet temperature and pressure conditions, for an input power of 9W, as seen in Figure 8. Based on Figure 8a, the thrust produced is dependent on the inlet pressure and is not significantly affected by the inlet temperature. From Figure 8b, the specific impulse is found to be almost constant below the saturation point and varies between 117 to 119 s. This is likely because chamber exit temperature does not significantly vary when the inlet temperature is below the saturation point.

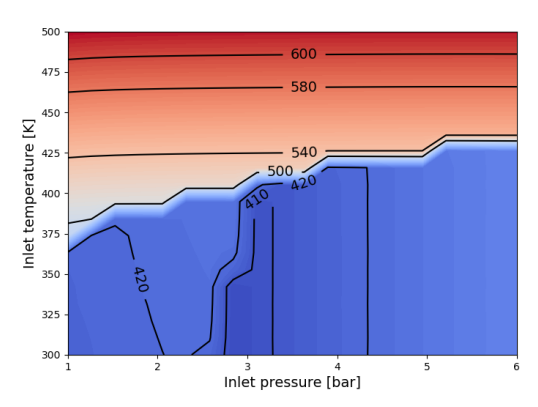


Figure 7a. Input power = 1 W

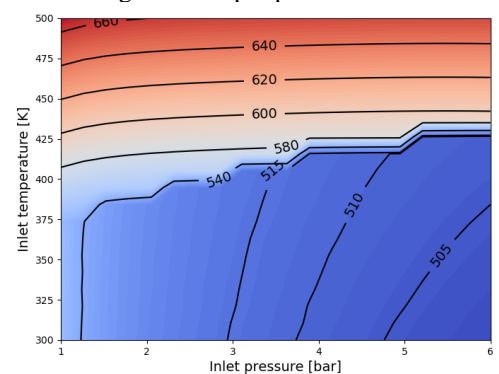


Figure 7b. Input power = 4 W

IAC-24,E2,1,1,x84841 Page 8 of 15

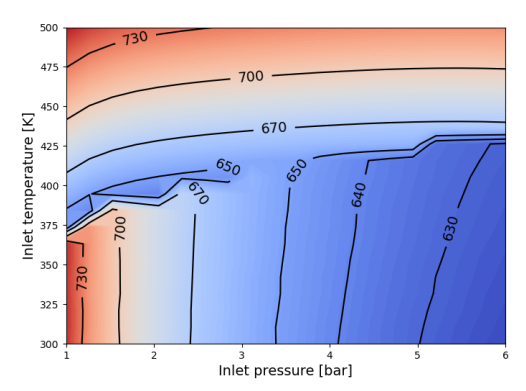


Figure 7c. Input power = 9 W

Figure 7. Chamber exit temperature contour plots for varying inlet temperature, pressure and input power

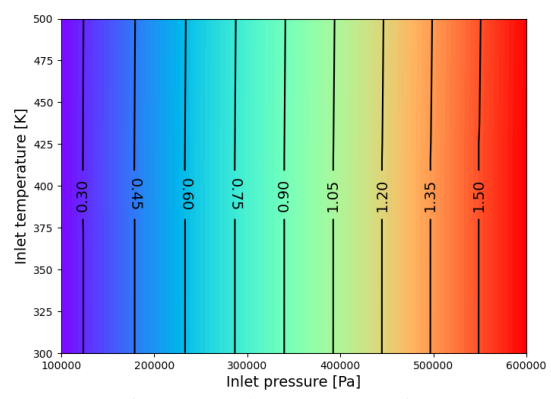


Figure 8a. Thrust contour (in mN)

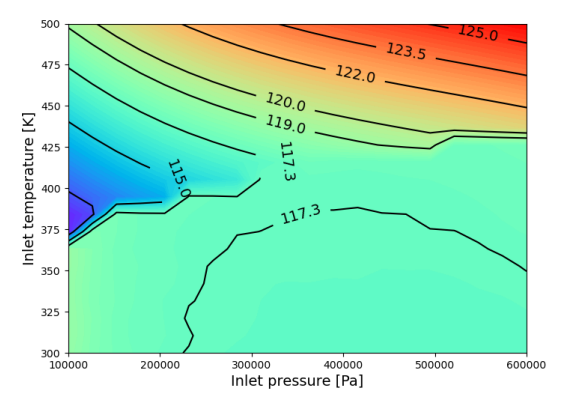


Figure 8b. Specific impulse contour (in s)

Figure 8. Thrust and specific impulse contour plots for varying inlet temperature and pressure

These results gave an idea of how input operating conditions given to the model have an effect on the output parameters. It also gives an understanding of how the modelling of the heating chamber influences the thruster performance, especially with the sharp changes in exit conditions with a change in inlet temperature and input power.

3.1.3 VLM nozzle loss factors

The loss factors in the nozzle model depended on various geometric parameters and operating conditions which were inter-dependent. Hence, each case was analysed separately. First, the geometric parameters varied while keeping the operating conditions constant and vice-versa.

In the first case, the chamber exit temperature was varied between 300 to 600 K and the pressure was varied between 1 and 6 bar. A constant throat width of 45 μm and a nozzle exit width of 500 μm were used. For the second case, the width of the nozzle throat was varied between 30 and 90 μm while the width of the nozzle exit was varied between 300 and 900 μm . A constant chamber pressure of 5 bar and a temperature of 500 K were used as the operating conditions.

From Figure 9a, it was observed that the discharge coefficient contour lines were horizontal, indicating that it only depended on the nozzle throat width and increased with an increase in throat width. The Isp-efficiency on the other hand, was clearly a function of both the throat width and the width of the exit, as seen in Figure 9b. An interesting observation was that the Isp-efficiency increased in value with an increase in nozzle exit width, but the gradient of the contour lines decreased considerably. One interpretation of this result was that there was a particular nozzle exit width that provided maximum Isp-efficiency.

To check whether this maximum value changed with other parameters, the chamber pressure, temperature and other geometric parameters were altered to see the results. It was found that only with a change in the length of the divergent section of the nozzle did the nozzle exit width change, corresponding to the maximum Ispefficiency.

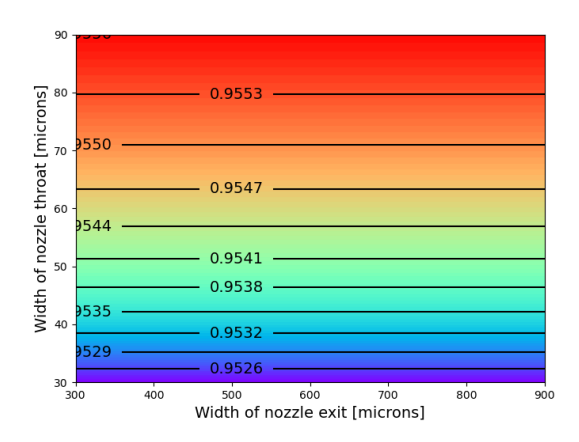


Figure 9a. Discharge coefficient contour

IAC-24,E2,1,1,x84841 Page 9 of 15

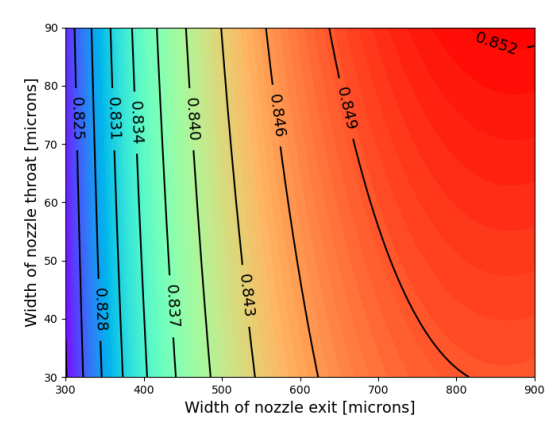


Figure 9b. Isp-efficiency contour

Figure 9. Contour plots for varying geometry and constant operating conditions.

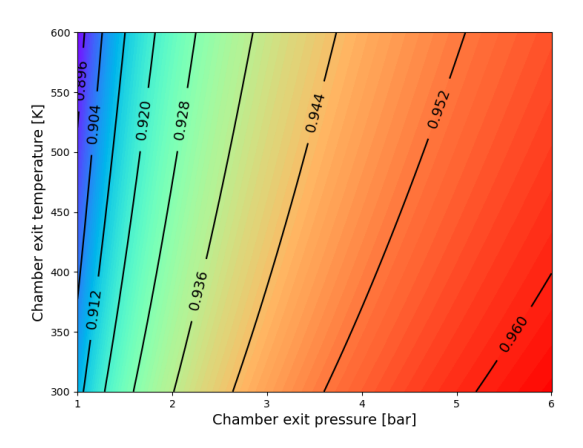


Figure 10a. Discharge coefficient contour

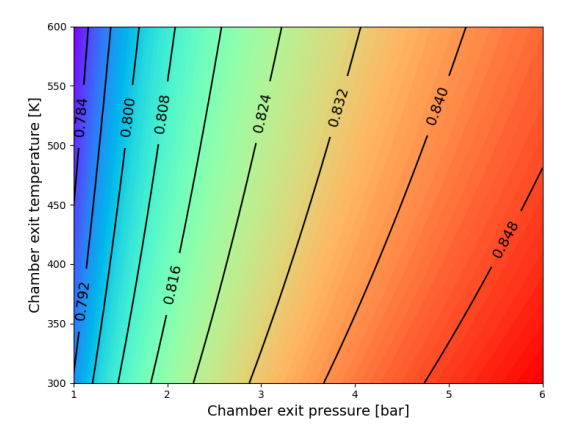


Figure 10b. Isp-efficiency contour

Figure 10. Contour plots for varying operating conditions and constant geometry.

It was observed that as the length of the divergent section was increased, the width of the nozzle exit at which the maximum Isp-efficiency was predicted also increased. This implied that the correlation used for Isp-efficiency predicted significantly different values for small changes in the nozzle length and width and hence, it was concluded that Isp-efficiency was strongly correlated with the nozzle geometry.

Further, from Figure 10a and Figure 10b, it was clear that both discharge coefficient and Isp-efficiency increase with an increased for higher chamber exit pressures and lower exit temperatures.

3.2 Results of the LPM thruster model

The geometry used to analyse the analytical model for the LPM thruster was obtained from the work of D.C Guerrieri [20] who had worked on using two configurations with either heated slots or channels for his design. The dimensions of the configurations are provided in Table 5.9. The number of slots and channels was chosen such that the effective cross-sectional area remained the same in either case. Based on Equations (12) and (13), the transmission coefficient for the slot and channel geometries were calculated to be 0.3565 and 0.754, respectively. The propellant used was water, with reasons similar to that given for the VLM thruster. The properties considered are provided in Table 3. Based on Equation (16), the accommodation coefficient was evaluated to be 0.86.

First, a comparison was made between the two models with and without the use of the accommodation coefficient. The wall temperature was varied between 300 and 900 K and the thrust and specific impulse were calculated at three plenum pressure values of 300 Pa, 500 Pa and 700 Pa., and at a plenum temperature of 300 K.

Table 3. Geometrical parameters of LPM thruster

Parameter	Value
Length of slot (mm)	0.5
Width of slot (mm)	5.375
Height of slot (mm)	0.1
No. of slots	44
Length of channel (mm)	0.5
Diameter of channel (mm)	0.1
No. of channels	3036

The resulting plots of the thrust and specific impulse for the slot and channel geometries are plotted in Figure 11 and Figure 12, respectively. It was observed that as the plenum pressure increased, the thrust generated also increased, however, the specific impulse did not change. This is in agreement with the governing equations used to calculate the parameters. Further, the thrust produced

IAC-24,E2,1,1,x84841 Page 10 of 15

by the slot geometry for a particular set of plenum pressure and wall temperature values was higher than the corresponding thrust produced by the channel geometry. This was purely due to the difference in the calculated transmission coefficient of the respective geometries.

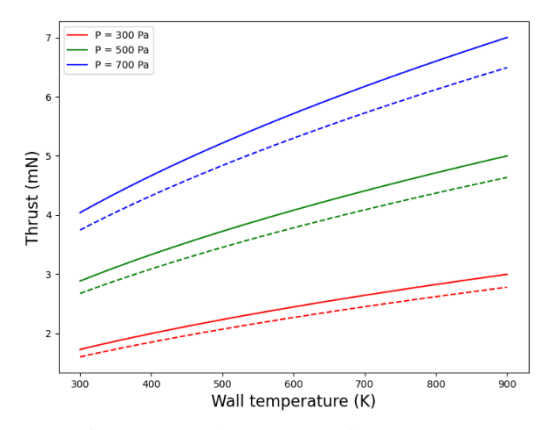


Figure 11a. Thrust v.s wall temperature

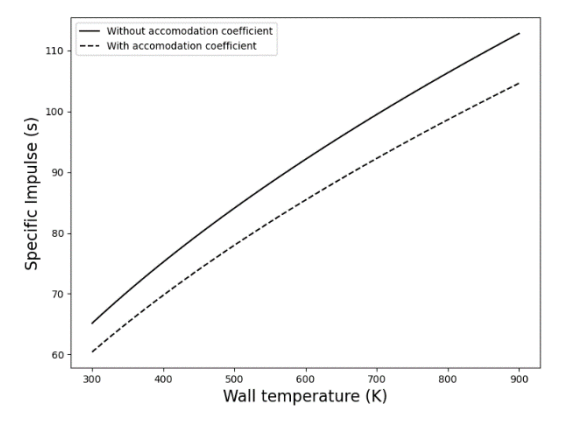


Figure 11b. Specific impulse v.s wall temperature

Figure 11. Performance plots for slot geometry

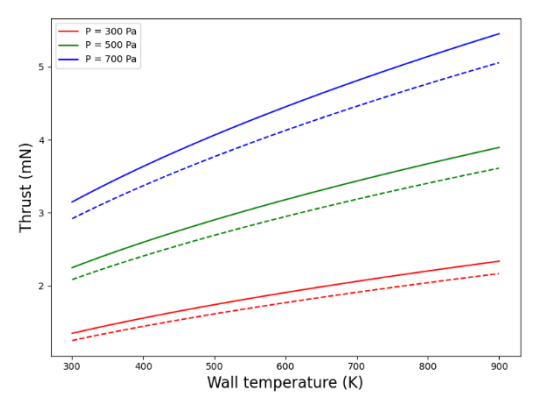


Figure 12a. Thrust v.s wall temperature

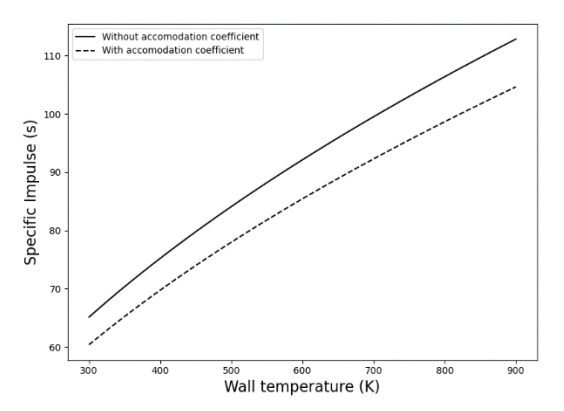


Figure 12b. Specific impulse v.s wall temperature

Figure 12. Performance plots for channel geometry.

Lastly, it was observed that for both the slot and channel geometries, the thrust and specific impulse were reduced by 7.26 % due to the accommodation coefficient. This meant that due to a certain amount of heat loss within the thruster, the performance was reduced by 7.26 % relative to a scenario where the losses would not have occurred. The general conclusion from these results was that the inclusion of the thermal accommodation reduced the performance of the thruster as expected.

3.3 Optimal points

To understand how the developed analytical models could be applied to determining the optimal operating points of the VLM and LPM thrusters, a simple optimization problem was demonstrated. This was done with the help of an objective function. This function took the weighted average of certain normalized parameters and produced a value between 0 and 100. This was considered to be a maximization problem and hence, a higher value of the objective function implied a more optimal operating point.

Equation (20) is used to normalize the parameter f which has a maximum and minimum value of f_{max} and f_{min} , respectively, in the entire domain. This was used instead of taking the ratio of f to f_{max} in order to remove any bias towards one particular parameter.

$$\bar{f} = \frac{f - f_{min}}{f_{max} - f_{min}} \tag{20}$$

As a baseline, certain requirements of the Delfi-PQ propulsion system [26] were assumed to be the requirements of the thruster, as provided in Table 4. Delfi-PQ propulsion system requirements. Further, it was assumed that the application of the thruster would be for station-keeping of Low Earth Orbit (LEO) satellites. This would mean that a delta-V requirement would also exist based on the given satellite and propellant mass on board. This would imply a dependency on the mass flow rate

IAC-24,E2,1,1,x84841 Page 11 of 15

and specific impulse, based on which the required delta-V can be defined. Based on these factors, the parameters considered were the normalized values of thrust to power ratio $\overline{TP_{ratio}}$, specific impulse \overline{Isp} and the mass flow rate $\dot{\overline{m}}$.

For the VLM thruster, an added parameter was the inlet pressure $\overline{P_0}$, since minimizing the operating pressure would be more favourable in a thruster with relatively high operating pressure. For a known mass of the satellite and propellant mass, the delta-V produced by the thruster would be proportional to the specific impulse and hence, a higher delta-V requirement would reflect in a higher specific impulse requirement. The mass flow rate would indirectly represent the burn duration of the thruster. It is assumed that the burn duration would need to be minimised to make the required manoeuvre of the satellite as fast as possible. This could be done by maximising the flow rate. Based on the considered requirements and parameters, the objective functions used for the model of the VLM and LPM thrusters are shown in Equations (21) and (22).

$$obj_{VLM} = \frac{\left(W_{\nu_1} \overline{TP_{ratio}} + W_{\nu_2} \overline{I_{sp}} + W_{\nu_3} \overline{m} + W_{\nu_4} (1 - \overline{P_0})\right)}{\sum W_{\nu}} X100$$
 (21)

$$obj_{LPM} = \frac{\left(W_{l_1} \overline{TP_{ratio}} + W_{l_2} \overline{I_{sp}} + W_{l_3} \overline{m}\right)}{\sum W_l} X100$$
 (22)

Table 4. Delfi-PQ propulsion system requirements

Requirement Relevance

The thrust provided by the Upper limit for the propulsion system shall be 3 mN working range of the as a maximum.

LPM thruster.

The thrust provided by the Lower limit for the propulsion system shall be at working range of least 0.12 mN. the LPM thruster.

The micro-propulsion system shall have at least two modes: idle with max. power consumption 15 mW, and full Constraint for the thrust with max. power maximum input consumption 4W. power.

The weights were determined based on expert opinions taken from professors and researchers working in this field. A separate set of weights were also assigned to the opinions of experts based on their qualification levels. The averaged weights used were as shown in Table 5.

Table 5. Weights for the objective functions

$W_{v_1} = 5$ $W_{v_2} = 5$	$W_{l_1} = 5$ $W_{l_2} = 4$
$W_{v_3} = 4$ $W_{v_4} = 2$	$W_{l_3} = 2$

3.3.1 Optimal operating points for the VLM thruster

For the VLM thruster, the baseline geometry used was the large serpentine channel with a long nozzle section which was worked on by M.D Silva [9]. The objective function was calculated for a range of inlet pressures varying from 1.5 to 6 bar and input power varying from 1 to 9 W. Five cases were calculated with different inlet temperatures which were chosen arbitrarily to include the effect of all considered constraints. The active constraints in the problem included a maximum thrust requirement of 3mN and a minimum thrust requirement of 0.12 mN. Based on the initial requirements, the maximum input power required was 4W, however, to get a better understanding of the variation of the objective function over a larger range of values, the limit of 9W was considered. Lastly, the limits of the chamber exit temperature were maintained between the saturation temperature of the propellant and 90 % of the critical temperature of the propellant. The contour plots of the objective function obtained for the VLM thruster are shown in Figure 13.

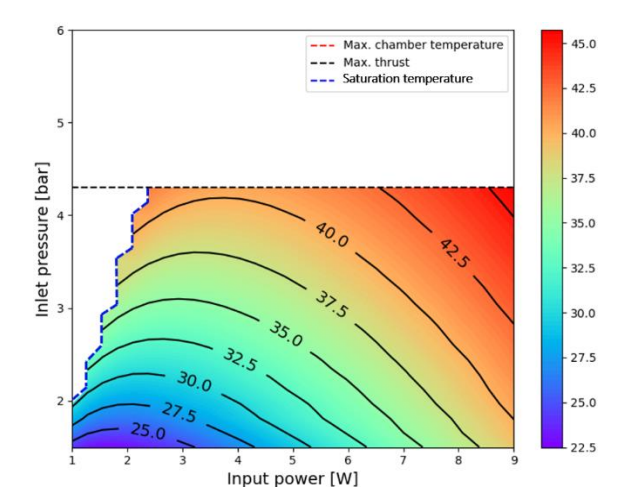


Figure 13a. Inlet temperature = 384 K

IAC-24,E2,1,1,x84841 Page 12 of 15

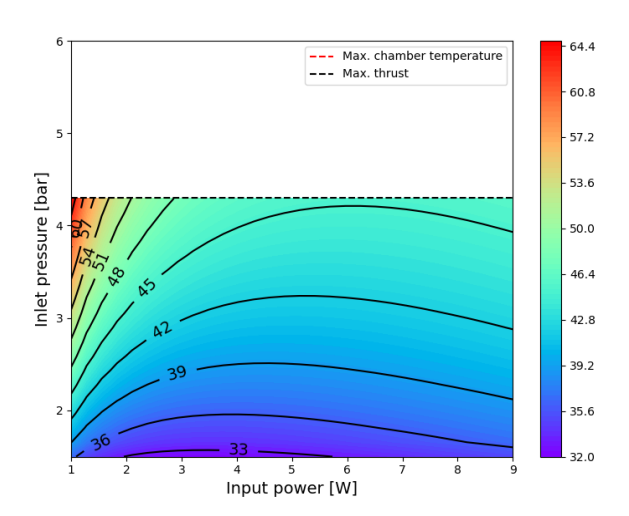


Figure 13b. Inlet temperature = 426 K

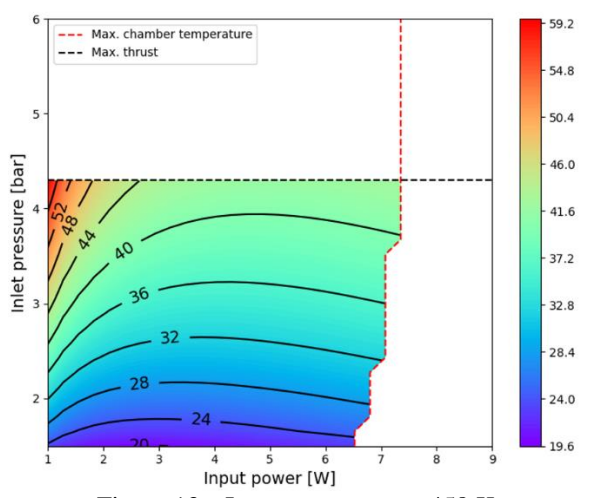


Figure 13c. Inet temperature = 458 K

Figure 13. Contour plots for the objective function defined for the VLM thruster for different inlet temperature values. "Max. thrust" and "Max input power" denote the maximum thrust and power constraints defined by the requirements.

From the plot in Figure 13a, it was observed that the contours of the objective function were constrained by the maximum thrust requirement and the saturation temperature curve. The values increased with both inlet pressure and input power and its highest value was found to be at an input power of 9 W and an inlet pressure of 4.293 bar. However, the values also increased for lower input power values, which indicated that there was a region where the function had a minimum value. Due to this, when the input power was constrained to a maximum of 4 W, it was found that the optimal point occurred at an input power of 2.379 W. Further, the limit defined by the saturation temperature curve shifts to the left with an increase in inlet temperature. This can be

explained by the fact that the power required to increase the propellant temperature becomes lower when the inlet temperature is increased.

The plot in Figure 13b shows a case wherein the propellant was in the vapour phase at the inlet for inlet pressure values up to a value of 4.293 bar. The maximum value of the objective was found at this pressure and for an input power of 1 W. For the plot in Figure 13c, the constraint applied on the chamber exit temperature is active and restricts the feasible region of the objective. The value of the objective is again seen to be highest at low input power values and high inlet pressures. As the input power is increased, the constraint applied on the chamber exit temperature shifts to the left, indicating that an increase in power proportionally increases the chamber temperature.

The most realistic operating point where the performance of the VLM thruster may be optimised can be obtained from Figure 13a with an inlet pressure of 4.293 bar and an input power of 9 W.

3.3.2 Optimal operating points for the LPM thruster

The objective function for the LPM thruster was calculated for a range of plenum pressures from 3 to 1500 Pa and wall temperature values ranging from 350 to 900 K. The plenum temperature was assumed to be constant and equal to 300 K. The active constraints in the problem included the same constraints used for the VLM thruster, except that the limit on the input power of 4 W was included in this case. The contour plots for the objective function for the two geometric configurations used, i.e., the slot geometry and channel geometry, were plotted as shown in Figure 14a and Figure 14b, respectively. It was observed that the constraints of minimum and maximum thrust restrict the feasible region to certain limits of the plenum pressure.

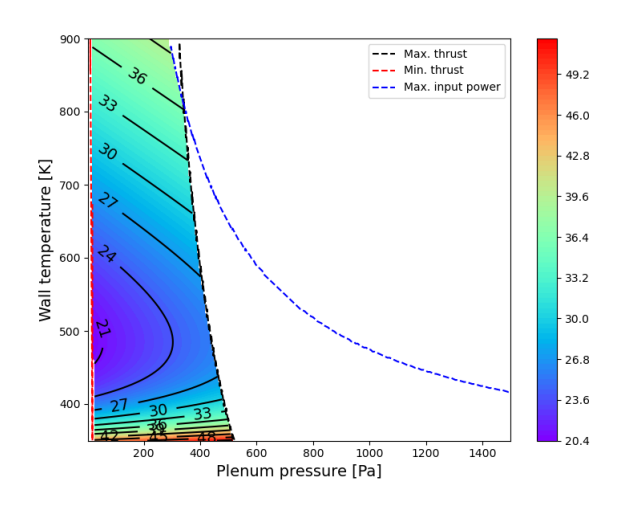


Figure 14a. Slot geometry

IAC-24,E2,1,1,x84841 Page 13 of 15

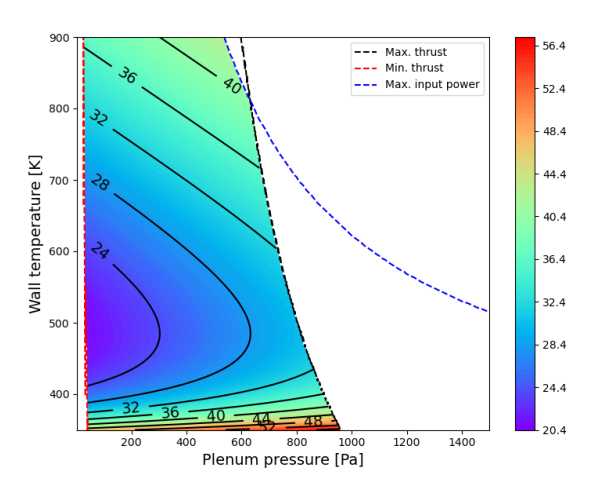


Figure 14b. Channel geometry

Figure 14. Contour plots for the objective function defined for the LPM thruster for the slot and channel geometries. "Max. thrust", "Min. thrust" and "Max input power" denote the maximum thrust, minimum thrust, and power constraints defined by the requirements.

Further, the constraint on the maximum input power intersects with the curve limiting the maximum thrust.

For the channel geometry, the maximum plenum pressure that can be used within the constraints is higher than that for the slot geometry. The objective function itself seems to increase with both wall temperature and pressure. However, very high values are obtained at lower plenum pressures and wall temperatures. This is considered to be due to the very low wall temperatures used that are close to the value of the plenum temperature. When the wall temperature is considered equal to the plenum temperature, the thruster would effectively act as a cold gas thruster with the performance purely depending on the plenum pressure. The results in this region are not considered for the LPM thruster, but it was interesting to note that this region had a higher objective function value than the LPM thruster, implying that the cold gas concept may be more optimal.

The optimal operating point for the LPM thruster was found to be at a wall temperature of 900 K for both geometries and a plenum pressure of 288.859 Pa for the slot geometry and 537.106 Pa for the channel geometry.

4. Conclusions

The current study involved the development of a set of analytical models to accurately predict the performance of Vaporized Liquid Micro-reistojet (VLM) and Low Pressure Micro-resistojet (LPM) thrusters for a given set of geometric configurations and operational conditions. A need was identified to build an improved analytical model that would overcome the deficiencies of

previous models to better determine the optimal operating points of the thruster to be tested for demonstration missions.

An analytical model was set up for the VLM thruster with a one-dimensional model used to represent the heating chamber section. The nozzle section was modelled with the use of Ideal Rocket Theory along with a set of correlations used to predict the loss factors. The LPM thruster was modelled using the concepts of rarefied gas dynamics and included a correlation for the accommodation coefficient to account for the efficiency of heat transfer from the thruster walls.

The results obtained from applying the developed analytical models for the VLM thruster revealed that the differences in the nozzle configurations produced a larger difference in the thruster performance than a change in the chamber geometry. Analysing the effect of operating conditions on thruster performance revealed that the inlet temperature and input power caused significant changes to the output, especially when the fluid was saturated at the inlet. Further, the nozzle loss factors were found to have a strong correlation with the nozzle geometry. On the other hand, the results for the LPM thruster model showed that the inclusion of the accommodation coefficient in the model reduced the thrust and specific impulse predictions.

The models were then applied to a sample optimization problem. Based on a set of requirements and constraints, the optimal operating points of the VLM and LPM thrusters were estimated over a range of operating conditions. It was found that the optimal operating point of the VLM was at an inlet pressure of 4.293 bar and an input power of 9W while the optimal point for the LPM thruster was at a plenum pressure of 288.859 Pa for the slot geometry and 537.106 Pa for the channel geometry, at a wall temperature of 900 K.

Acknowledgements

I would like to thank Dr. Angelo Cervone, Associate Professor at TU Delft, for his guidance and supervision throughout the project.

References

- [1] H. P.-S. J. Heidt, A. S. Moore, S. Nakasuka and R. J. Twiggs, "CubeSat: A New Generation of Picosatellite for Education and Industry Low-Cost Space Experimentation," in *Engineering Education, Physics*, 2000.
- [2] D. Selva and D. Krejci, "A survey and assessment of the capabilities of Cubesats for Earth observation," *Acta Astronautica*, vol. 74, no. 0094-5765, pp. 50-68, 2012.

IAC-24,E2,1,1,x84841 Page 14 of 15

- [3] A. H. Poghosyan and A. Golkar, "CubeSat evolution: Analyzing CubeSat capabilities for conducting science missions," *Progress in Aerospace Sciences*, vol. 88, pp. 59-83, 2017.
- [4] R. Twiggs, Making it Small, San Luis Obispo: Cal Poly Developer's Workshop, 2009.
- [5] A. Cervone, D. C. Guerrieri, M. D. A. C. E. Silva and F. Leverone, "Electrothermal Microthruster," Space Micro-propulsion for Nanosatellitess: Progress, Challenges and Future, pp. 125-149, 2022.
- [6] V. Pallichadath, L. Turmaine, A. Melaika, S. Gelmi, M. V. Ramisa, D. Rijlaarsdam, M. Silva, D. Guerrieri, M. Uludag, B. Zandbergen and A. Cervone, "In-orbit micro-propulsion demonstrator for PICO-satellite applications," *Acta Astronautica*, vol. 165, no. 0094-5765, pp. 414-423, 2019.
- [7] J. Mueller, "A review and applicability assessment of MEMS-based microvalve technologies for microspacecraft propulsion," in *American Institute of Aeronautics and Astronautics*, 2012.
- [8] J. Cen, "Performance evaluation and flow visualization of a MEMS based vaporizing liquid micro-thruster," *Acta Astronautica*, vol. 67, pp. 468-482, 2010.
- [9] M. d. A. C. e. Silva, "MEMS Micropropulsion: Design, Modeling and Control of Vaporizing Liquid Microthrusters," Delft University of Technology, 2018.
- [10] A. Ketsdever, D. Wadsworth, S. Vargo and E. Muntz, "A Free Molecule Micro-Resistojet: An Interesting Alternative to Nozzle Expansion," Air Force Research Laboratory (AFMC), 1998.
- [11] S. Radu, M. Uludag, S. Speretta, J. Bouwmeester, E. Gill and N. C. Foteinakis, "Delfi-PQ: The first pocketqube of Delft University of Technology," in *Proceedings of 69th International Astronautical Congress*, 2018.
- [12] T. L. Bergman, A. S. Lavine, F. P. Incropera and D. P. DeWitt, Fundamentals of Heat and Mass Transfer, John Wiley and Sons.
- [13] Y. A. Cengel and J. M. Cimbala, Fluid Mechanics Fundamentals and Applications, McGraw-Hill Publications, 2013.
- [14] C. Hanselaar, "Evaporative Two-Phase Micro-Flow Modelling," Delft University of Technology, 2016.
- [15] X. Peng and G. Peterson, "Convective heat transfer and flow friction for water flow in

- microchannel structures," *International Journal of Heat and Mass Transfer*, vol. 39, no. 12, pp. 2599-2608, 1996.
- [16] N. M. Kulava and H. G.A., "Supersonic nozzle discharge coefficients at low Reynolds numbers," *AIAA Journal*, vol. 9, no. 9, pp. 1876-1879, 1971.
- [17] M. D. Giorgi and D. Fontanarosa, "A novel quasi-one-dimensional model for performance estimation of a Vaporizing Liquid Microthruster," *Aerospace Science and Technology*, vol. 84, pp. 1020-1034, 2019.
- [18] D. Whitfield, "Integral solution of compressible turbulent boundary layers using improved velocity profiles," ARO, Inc., Arnold Air Force Station, TN, 1978.
- [19] A. Cervone, A. Mancas and B. Zandbergen, "Conceptual design of a low-pressure microresistojet based on a sublimating solid propellant," *Acta Astronautica*, vol. 108, pp. 30-39, 2015.
- [20] D. C. Guerrieri, M. d. A. C. e. Silva, A. Cervone and E. Gill, "An analytical model for characterizing the thrust performance of a Low-Pressure Micro-Resistojet," *Acta Astronautica*, vol. 152, pp. 719-726, 2018.
- [21] A. D. Ketsdever, R. H. Lee and T. C. Lilly, "Performance testing of a microfabricated propulsion system for nanosatellite applications," *Journal of Micromechanics and Microengineering*, vol. 15, no. 12, pp. 2254-2263, 2005.
- [22] J. M. Lafferty, Foundations of Vacuum Science and Technology, John Wiley and Sons, 1998.
- [23] A. Chandra, "Response Surface Based Design Optimization of a Low-Pressure Microresistojet's Heat Exchanger," Delft University of Technology, 2021.
- [24] L. Tengfei, "Numerical study of gas-surface interaction models for micro scale rarefied gas flow simulation," Hong Kong University of Science and Technology, 2015.
- [25] D. C. Guerrieri, M. d. A. C. e. Silva, A. Cervone and E. Gill, "Selection and Characterization of Green Propellants for Micro-Resistojets," *Journal of Heat Transfer*, vol. 139, p. 102001, 2017.
- [26] Delfi-PQ, Propulsion Subsystem Requirements for the Delfi-PQ Satellites, Delft University of Technology, 2017

IAC-24,E2,1,1,x84841 Page 15 of 15